Spin Waves and magnetic exchange interactions in insulating Rb_{0.89}Fe_{1.58}Se₂

Miaoyin Wang, Chen Fang, Dao-Xin Yao, GuoTai Tan, Leland W. Harriger, Yu Song, Tucker Netherton, Chenglin Zhang, Meng Wang, Matthew B. Stone, Wei Tian, Jiangping Hu, and Pengcheng Dai, 6, 5, *

Department of Physics and Astronomy, The University of Tennessee, Knoxville, Tennessee 37996-1200, USA

Department of Physics, Purdue University, West Lafayette, Indiana 47907, USA

State Key Laboratory of Optoelectronic Materials and Technologies,
Sun Yat-sen University, Guangzhou 510275, China

College of Nuclear Science and Technology, Beijing Normal University, Beijing 100875, China

Beijing National Laboratory for Condensed Matter Physics and Institute of Physics,
Chinese Academy of Sciences, P. O. Box 603, Beijing 100190, China

Neutron Scattering Science Division, Oak Ridge National Laboratory, Oak Ridge, Tennessee 37831-6393, USA

Ames Laboratory and Department of Physics and Astronomy Iowa State University, Ames, Iowa 50011, USA

The discovery of alkaline iron selenide AFe_{1.6+x}Se₂ (A = K, Rb, Cs) superconductors [1-5] has generated considerable excitement in the condensed matter physics community because superconductivity in these materials may have a different origin from the sign reversed s-wave electron pairing mechanism [6-8], a leading candidate proposed for all other Fe-based superconductors [9, 10]. Although $AFe_{1.6+x}Se_2$ are isostructural with the metallic antiferromagnetic (AF) iron pnictides such as $(Ba,Ca,Sr)Fe_2As_2$ [11, 12], they are insulators near x = 0 [3–5] and form a $\sqrt{5} \times \sqrt{5}$ blocked AF structure (Fig. 1a) completely different from the iron prictides [3, 13, 14, 16, 17]. If magnetism is responsible for superconductivity of all iron-based materials [10], it is important to determine their common magnetic features. Here we use neutron scattering to map out spin waves in the AF insulating Rb_{0.89}Fe_{1.58}Se₂. We find that although $Rb_{0.89}Fe_{1.58}Se_2$ has a Néel temperature $(T_N = 475 \text{ K})$ much higher than that of the iron pnictides $(T_N \leq 220 \text{ K})$, spin waves for both classes of materials have similar zone boundary energies [18-20]. A comparison of the fitted effective exchange couplings using a local moment Heisenberg Hamiltonian in $Rb_{0.89}Fe_{1.58}Se_2$, $(Ba,Ca,Sr)Fe_2As_2$ [18–20], and iron chalcogenide Fe_{1.05}Te [21] reveals that their next nearest neighbor (NNN) exchange couplings are similar. Therefore, superconductivity in all Fe-based materials may have a common magnetic origin that is intimately associated with the NNN magnetic exchange interactions, even though they have metallic or insulating ground states, different AF orders and electronic band structures.

Soon after the discovery of superconductivity in iron pnictides [22], calculations and experiments have found that electronic band structures of these materials are composed of hole and electron Fermi pockets near $\Gamma(0,0)$

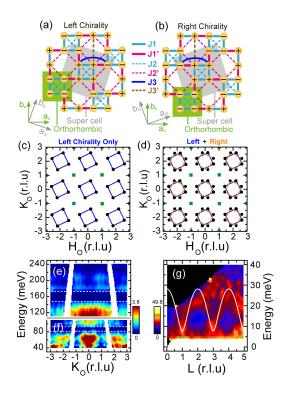
and M(1,0)/M(0,1) points, respectively [10]. As a consequence, sign reversed quasiparticle excitations between the hole and electron pockets can induce s^{\pm} -wave superconductivity, giving rise to a neutron spin resonance at the in-plane wave vector Q = (1,0) (Fig. 1c) [23– 25]. If sign reversed electron-hole pocket excitations between $\Gamma(0,0)$ and M(1,0)/M(0,1) points are necessary for superconductivity, superconductivity in alkaline iron selenides should have a different microscopic origin since angle resolved photoemission experiments measurements on these materials reveal only electron Fermi surfaces at M(1,0)/(0,1) points and no hole Fermi pockets at $\Gamma(0,0)$ point [6–8]. On the other hand, if AF spin excitations are responsible for superconductivity in Fe-based superconductors [10, 26], one would expect that spin waves in the parent compounds of different classes of Fe-based superconductors have a common magnetic origin associated with superconductivity. Previous work on spin waves of $(Ba,Ca,Sr)Fe_2As_2$ [18–20] and $Fe_{1.05}Te$ [21] suggests that the NNN exchange couplings in these materials are similar. Since the insulating $AFe_{1.6+x}Se_2$ has completely different magnetic structure and static ordered moment (Fig. 1) from those of (Ba,Ca,Sr)Fe₂As₂ and Fe_{1.05}Te [11], it is important to determine if its effective magnetic exchange couplings are similar to these materials.

Here we report inelastic neutron scattering studies of spin waves in the insulating $Rb_{0.89}Fe_{1.58}Se_2$ with $T_N =$ 475 K. Our neutron diffraction measurements on the sample confirmed the previously proposed Fe₄ block AF checkerboard structure (Fig. 1a) [3]. Since the ferromagnetic (FM) Fe₄ block in the $\sqrt{5} \times \sqrt{5}$ superlattice unit cell can have either left or right chirality (Figs. 1a and 1b), one expects to observe four AF Bragg peaks stemming from each of the chiralities. Figure 1c shows the expected AF peaks from the left chirality in reciprocal space using the orthorhombic unit cell similar to that of iron prictides [18–20], where they occur at $(H_o, K_o, L_o) = (0.2 + m, 0.6 + n, L_o); (-0.2 + m, -0.6 + m, -0.6 + m, L_o); (-0.2 + m, -0.6 + m, -0.6$ $n; L_o$; $(0.6 + m, -0.2 + n, L_o); (-0.6 + m, 0.2 + n, L_o)$ $(m, n = \pm 2, \pm 4, \cdots, \text{ and } L_o = \pm 1, \pm 3, \cdots)$. Considering both chiralities for the AF order, there are eight Bragg

peaks at wave vectors $(H_o, K_o, L_o) = (\pm 0.2 + m, \pm 0.6 + n, L_o)$ and $(H_o, K_o, L_o) = (\pm 0.6 + m, \pm 0.2 + n, L_o)$ from the block AF checkerboard structure (Fig. 1d), where the odd values of L_o indicate AF coupling along the c-axis direction [3, 16, 17]. Therefore, acoustic spin waves in the AF ordered phase of Rb_{0.89}Fe_{1.58}Se₂ should stem from these eight Bragg peaks.

Before mapping out the wave vector dependence of spin waves in Rb_{0.89}Fe_{1.58}Se₂, we first determine their overall energy bandwidth and the effective c-axis coupling. Figures 1e and 1f show the background subtracted scattering projected in the wave vector $(Q = [-1.5, K_o])$ and energy plane. One can see three clear plumes of scattering arising from the in-plane AF zone centers Q = (0, -2), (0, 0),and (0,2) rlu. With increasing energy, spin waves are gapped at energies between 75 and 95 meV (Fig. 1f) and between 150 and 170 meV (Fig. 1e). The zone boundary spin wave energies are around 220 meV (Fig. 1e). Therefore, in spite of the large differences in Néel temperatures of $Rb_{0.76}Fe_{1.6}Se_2$ ($T_N = 475 \text{ K}$) [3, 16, 17], $(Ba,Ca,Sr)Fe_2As_2 (T_N \le 220 \text{ K}) [18-20], \text{ and } Fe_{1.05}Te$ $(T_N \approx 70 \text{ K})$ [21], their zone boundary spin wave energies are rather similar. To estimate the AF coupling strength along the c-axis, we show in Fig. 1g spin waves projected in the wave vector $Q = [0.6, 0.2, L_o]$ and energy space. One can see clear dispersive spin waves stemming from AF positions $L_o = 1, 3, 5$ that reach the zone boundary energy near 30 meV.

To see the evolution of spin waves with increasing energy, we show in Fig. 2 the two-dimensional constantenergy (E) images of spin waves in the $[H_o, K_o]$ plane for various incident beam energies (E_i) . From their caxis dispersion (Fig. 1g), we know that spin waves in $\mathrm{Rb}_{0.89}\mathrm{Fe}_{1.58}\mathrm{Se}_{2}$ are three-dimensional similar to that in (Ba,Ca,Sr)Fe₂As₂ [18–20] and center at AF wave vectors $Q_{AF} = (H_o, K_o, L_o) = (\pm 0.2 + m, \pm 0.6 + n, L)/(\pm 0.6 + m, L)$ $m, \pm 0.2 + n, L)$ with $L_o = \pm 1, \pm 3, \cdots$ rlu. For an energy transfer of $E = 10 \pm 2$ meV (above the anisotropy gap of E = 8 meV, see supplementary information), spin waves are peaked at the expected eight AF Bragg positions Q_{AF} around $Q=(0,0,\pm 1)$ rlu as shown in Fig. 2a. Upon increasing energies to $E=26\pm 2$ (Fig. 2b) and 30 ± 2 meV (Fig. 2c), spin waves from the two chiralities centered around the Q_{AF} positions become apparent and increase in size with increasing energy. The two spin wave rings from the left and right AF chiralities (Figs. 1a-1d) meet near $E=45\pm3$ meV (Fig. 2d). At $E=55\pm3$ meV, the overlapping spin waves from both AF chiralities still form rings around the Q_{AF} positions (Fig. 2e). Spin waves have evolved into broad rings centered around $(H_o, K_o, L_o) = (\pm m, \pm n, L_o)$ at $E = 70\pm 3$ meV as shown in Fig. 2f, just before disappearing into the $75 \le E \le 95$ meV spin gap (Fig. 1f). Upon re-emerging from the spin gap at an energy transfer of 110 ± 10 meV, spin waves form transversely elongated ellipses centered at the wave vectors $Q = (\pm 1, 0)/(0, \pm 1)$ (Fig. 2g), identical to the



The AF spin structure, reciprocal space, and caxis spin waves of the insulating Rb_{0.89}Fe_{1.58}Se₂. Our neutron scattering experiments were carried out on the ARCS chopper spectrometer at the Spallation Neutron Source, Oak Ridge National Laboratory. We co-aligned 2.7 g of single crystals grown by self-flux (with mosaic of $\sim 6^{\circ}$). The incident beam energies were $E_i = 80, 140, 250, 440 \text{ meV}$, and mostly with E_i parallel to the c-axis. Spin-wave intensities were normalized to absolute units using a vanadium standard (with 30% error). We define the wave vector Q at (q_x, q_y, q_z) as $(H_o; K_o; L_o) = (q_x a_o/2\pi; q_y a_o/2\pi; q_z c_o/2\pi)$ rlu, where $a_o = 5.65$ and $c_o = 14.46$ Å are the orthorhombic cell lattice parameters. The AF spin structures are shown for (a) left and (b) right chirality. The $\sqrt{5} \times \sqrt{5}$ superlattice structure is marked as grey with lattice parameter $a_s = 8.933$ Å. The orthorhombic lattice cell is shaded green. The effective NN, NNN, NNNN exchange couplings are marked as J_1/J_1' , J_2/J_2' , and J_3/J_3' , respectively. (c) The $[H_o, K_o]$ reciprocal space with the expected AF Bragg peaks from the left chirality. The green squares show nuclear Bragg peak positions. (d) Expected Bragg peaks for both chiralities. (e,f) Spin waves projected onto the K_o -E plane with H_o integration from -2 to -1. The scattering were measured with $E_i = 440,250 \text{ meV}$, respectively. (g) c-axis spin-wave dispersion projected on the L-E plane with H_o integration from 0.5 to 0.7 and K integration from 0 to 0.4. The solid line is the calculated c-axis dispersion using effective exchange couplings discussed in the main text.

AF ordering wave vector of (Ba,Ca,Sr)Fe₂As₂ [18–20]. Finally, at $E=200\pm20$ meV, an energy well above the $150\leq E\leq170$ meV spin gap, spin waves move into wave vectors $Q=(\pm1,\pm1)$ (Fig. 2h), almost identical to the zone boundary spin waves for BaFe₂As₂ [18] and Fe_{1.05}Te [21].

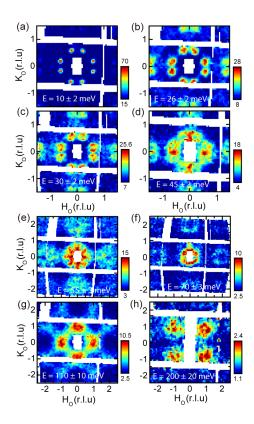


FIG. 2: Wave-vector dependence of spin-wave excitations at different energies in the $[H_o,K_o]$ scattering plane for $\mathrm{Rb_{0.89}Fe_{1.58}Se_2}$ at 10 K. Spin wave excitations at energies (a) $E=10\pm2$; (b) $E=26\pm2$; (c) $E=30\pm2$; (d) $E=45\pm3$; (e) $E=55\pm3$; (f) $E=70\pm3$; (g) $E=110\pm10$; and (h) $E=200\pm20$ meV. (a)-(c), (d)-(f),(g),(h) were obtained with $E_i=80$, 140, 250, and 440 meV, respectively, along the c-axis. The vertical color bars indicate intensity scale in mbarns/sr/meV/f.u.

We use a local moment Heisenberg Hamiltonian with the effective nearest (NN or J_1, J'_1), next nearest (NNN or J_2, J_2'), and next next nearest neighbor (NNNN or J_3,J_3') magnetic exchange couplings (Fig. 1a) to fit the observed spin-wave spectra [1, 27, 28, 30, 31]. To account for the ~ 8 meV low-energy spin gap, we add a spin anisotropy term J_s to align spins along the c-axis (see supplementary information). There are 8 spins in each magnetic unit cell (Figs. 1a and 1b), therefore we should have four spin wave bands in the Brillouin zone. From Figs. 1 and 2, we see that spin waves exist in three separate energy ranges: the lowest branch starts from ~ 9 meV to ~ 70 meV, second from ~ 80 meV to ~ 140 meV, and the third branch from \sim 180 meV to \sim 230 meV. The high quality of the spin-wave data allows us to place quantitative constraints on effective exchange couplings in the Heisenberg Hamiltonian (see supplementary information). While the low-energy spin waves between ~ 9 meV to ~ 70 meV are acoustic mode arising mostly from AF interactions of the FM blocked spins, the two other branches of excitations are optical spin waves associated

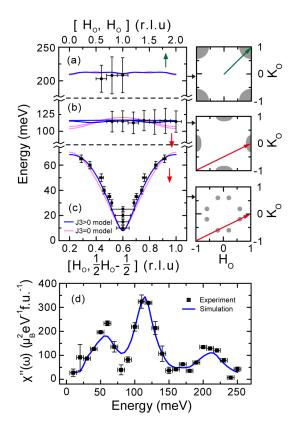


FIG. 3: Spin-wave dispersions of $Rb_{0.89}Fe_{1.58}Se_2$ and fits using Heisenberg Hamiltonian. Spin-wave dispersions obtained by cutting along high-symmetry directions marked in the right panels for (a) highest energy optical energy band; (b) medium energy optical energy band; and (c) acoustic spin wave mode. The blue solid lines show fits with $J_3 > 0$, while the pink solid lines are fits with $J_3 = 0$. (d) The energy dependence of the local susceptibility and our model calculation of the local susceptibility.

with exchange interactions of iron spins within the FM blocks [1, 28, 30, 31]. We have attempted, but failed, to fit the entire spin wave spectra using only the effective NN and NNN exchange coupling Heisenberg Hamiltonian (see Fig. 3 and supplementary information). For spinwave fits that include the NNNN exchange coupling J_3 , we find that the low energy spin wave band (acoustic band) depends mainly on J_1', J_2', J_3 , and J_c (the effective c-axis exchange coupling), but not J_1 and J_2 . The second band depends on the J_2 heavily and the top band is mainly determined by J_1 .

For simplicity, we consider each FM block with 4 aligned spins as a net spin S_{eff} . They interact with each other antiferromagnetically (via J_{eff}) to form a cuprates-like AF spin structure. There is one spin-wave band for this effective block-spin Heisenberg model, which has an analytical form for spin-wave dispersion (see supplementary information). By comparing the J_{eff} Heisenberg Hamiltonian with those of the J_1 - J'_1 - J_2 - J'_2 - J_3 - J'_3 model, we find that spin waves in the first band can be approx-

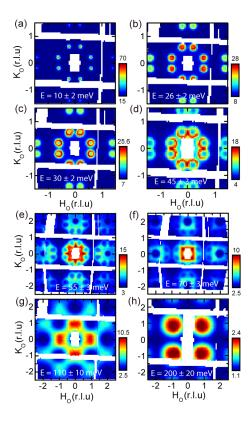


FIG. 4: Calculated wave-vector dependence of the spin waves in the $[H_o, K_o]$ scattering for identical energies as that of Fig. 2. The instrumental resolution is convoluted with the Heisenberg Hamiltonian.

imately described by the J_{eff} Heisenberg Hamiltonian, where $J_{eff}S_{eff}=(J_1'+2J_2'+2J_3)S/4$ is ~ 17 meV. This suggests that the low energy band is mainly determined by J_1',J_2',J_3 , and J_c . Physically, the lowest energy band corresponds to the block spin waves where the 4 spins fluctuate in phase and resemble a single spin. Only at high energies, the relative motions within the blocks can be excited, which correspond to the two high energy optical modes. Thus the high energy bands are basically determined by the intra-block couplings J_1 and J_2 .

To quantitatively determine the spin-wave dispersion, we determined the measured dispersion from a series of high symmetry scans through the (H_o, H_o, L_o) and $(H_o, 1/2H_o - 1/2, L)$ directions, where L_o was integrated to improve counting statistics. Figures 3a-3c summarize the dispersion of spin waves along the marked directions on the right panels. For the low-energy acoustic mode, we find a spin anisotropy gap below 8 meV and counter propagating spin waves for energies above 30 meV (Fig. 3c). The two high-energy optical spinwave modes are essentially dispersionless. The blue and pink solid lines show Heisenberg Hamiltonian fits to the dispersion curves with and without J_3 . The final fitted effective magnetic exchange couplings for spin-wave dispersions are $SJ_1 = -36 \pm 2$, $SJ'_1 = 15 \pm 8$, $SJ_2 = 12 \pm 2$,

 $SJ_2' = 16 \pm 5$, $SJ_3 = 9 \pm 5$, $J_3' = 0$, $SJ_c = 1.4 \pm 0.2$, and $SJ_s = 0.44 \pm 0.1$ meV (see supplementary information for fits with other parameters). Figure 3d shows energy dependence of the observed local susceptibility [4] and our calculation using the fitted parameters. We see that the calculated local susceptibility agrees quite well with the data. To further compare the data in Fig. 2 with calculated spin waves using fitted effective exchange couplings, we show in Figure 4 the two-dimensional spin-wave projections in the $[H_o, K_o]$ plane convoluted with instrumental resolution. The calculated spin-wave spectra capture all essential features in the data.

For a Heisenberg model with spin S, the total moment sum rule stipulates $M_0 = (g\mu_B)^2 S(S+1)$. For irons in the $3d^6$ electronic state, the maximum possible moment is $gS=4~\mu_B/{\rm Fe}$ for g=2, giving $M_0=24~\mu_B^2/{\rm Fe}$. Based on absolute spin wave intensity measurements in Fig. 3d, the sum of the fluctuating moments below $\sim\!250~{\rm meV}$ is $\langle m^2\rangle \approx 16\pm 3~\mu_B^2/{\rm Fe}$. If we assume that the ordered moment is on the order of $\sim\!3~\mu_B/{\rm Fe}$ [3, 16, 17], we see that the total moment sum rule is exhausted for magnetic scattering at energies below 250 meV. Therefore, spin waves in insulating Rb_{0.76}Fe_{1.63}Se₂ can be regarded as a classic local moment system where a Heisenberg Hamiltonian is an appropriate description of spin-wave spectra.

It is instructive to compare the effective magnetic exchange couplings in different iron-based superconductors. First, comparing $Rb_{0.89}Fe_{1.58}Se_2$ with $Fe_{1.05}Te$ [21], we note that although their static AF orders have completely different structures, these two iron chalcogenides are very similar in terms of the values of their effective exchange couplings. Both of them have: (i) large FM J_1 (or J_{1a}), (ii) large anisotropy between the two NN couplings $J_1(J_{1a})$ and J'_1 (or J_{1b}), (iii) AF NNN couplings and small anisotropy between two NNN couplings $J_2(\text{or},$ J_{2a}) and J'_{2} (or J_{2b}), and (iv) significant AF NNNN couplings J_3 . Therefore, the presence of the iron vacancy ordering in Rb_{0.89}Fe_{1.58}Se₂ reduces magnetic frustration and stabilizes the blocked AF structure, but does not change the local magnetic exchange couplings strengths as compared to $Fe_{1.05}$ Te [21]. Second, comparing ironchalcogenides to iron-prictides, we find that there are important differences as well as essential common features: the differences include the large FM J_{1a} and significant AF J_3 in iron-chalcogenides against the large AF J_{1a} and negligible J_3 in iron-prictides, respectively, and the common features include the large anisotropy of NN exchange couplings and similar AF NNN couplings. While the NN exchange couplings vary significantly according to the spin configurations between the corresponding two NN sites in the magnetically ordered states, the AF NNN exchange coupling remains almost uniform amongst different classes of materials even though their AF structures can be quite different. This is consistent with the idea that J_2 is mainly determined by a local superexchange

mechanism mediated by As or Se/Te [33]. Regarding the microscopic origin of superconductivity, the difference between the NN exchange couplings of the two classes of materials suggests that the NN FM exchange coupling cannot be responsible for superconductivity since electron pairing is in the spin singlet channel [34], which is not allowed by the FM coupling. However, the similarity on J_2 in both classes of materials suggests that if superconductivity in all Fe-based materials has a common magnetic origin, it must be intimately associated with the NNN magnetic exchange interactions, likely resulting in a s-wave pairing symmetry [35].

We thank Masaaki Matsuda for his help on triple-axis measurements discussed in the supplementary information. The neutron scattering work at UT is supported by the U.S. NSF-OISE-0968226, and by the U.S. DOE, Division of Scientific User Facilities (P.D.). The single crystal growth effort at UT is supported by U.S. DOE BES under Grant No. DE-FG02-05ER46202 (P.D.). Work at IOP is supported by the Chinese Academy of Sciences. D.X.Y. is supported by NSFC-11074310.

- * Electronic address: pdai@utk.edu
- [1] Guo, J. G. et al., Superconductivity in the iron selenide $K_xFe_2Se_2$ (0 $\leq x \leq 1.0$). Phys. Rev. B **82**, 180520(R) (2010).
- [2] Krzton-Maziopa, A. et al., Synthesis and crystal growth of $Cs_{0.8}(FeSe_{0.98})_2$: a new iron-based superconductor with $T_c = 27 \text{ K J. Phys.: Condens. Matter } \mathbf{23}, 052203 (2011).$
- [3] Fang, M. H. *et al.*, Fe-based high temperature superconductivity with $T_c = 31$ K bordering an insulating antiferromagnet in (Tl,K)Fe_xSe₂ Crystals. EPL,**94**, 27009 (2011).
- [4] Wang, A. F. et al., Superconductivity at 32 K in single crystal Rb_{0.78}Fe₂Se_{1.78}, Phys. Rev. B 83, 060512 (2011).
- [5] Wang, D. M., He, J. B., Xia, T.-L., and Chen, G. F., Effect of varying iron content on the transport properties of the potassium-intercalated iron selenide K_xFe_{2-y}Se₂. Phys. Rev. B 83, 132502 (2011).
- [6] Zhang,Y. et al., Heavily electron-doped electronic structure and isotropic superconducting gap in A_x Fe₂Se₂ (A = K, Cs), Nature Materials **10**, 273-277 (2011).
- [7] Qian, T. et al., Absence of holelike Fermi surface in superconducting K_{0.8}Fe1.7Se₂ revealed by ARPES, Phys. Rev. Lett. 106, 187001 (2011).
- [8] Mou, D. X. et al., Distinct Fermi Surface Topology and Nodeless Superconducting Gap in (Tl_{0.58}Rb_{0.42})Fe_{1.72}Se₂ Superconductor. Phys. Rev. Lett. 106, 107001 (2011).
- [9] Mazin, I. I., Iron superconductivity weathers another storm, Physics 4, 26 (2011).
- [10] Mazin, I. I., Superconductivity gets an iron boost. Nature 464, 183-186 (2010).
- [11] Johnston, D. C., The Puzzle of High Temperature Superconductivity in Layered Iron Pnictides and Chalcogenides. Advances in Physics 59, 803 (2010).
- [12] de la Cruz, C. et al., Magnetic order close to superconductivity in the iron-based layered ${\rm LaO}_{1-x}{\rm F}_x{\rm FeAs}$ sys-

- tems, Nature (London) 453, 899 (2008).
- [13] Häggström, L., Seidel, A., and Berger, R., A Mössbauer study of antiferromagnetic ordering in iron deficient TlFe_{2-x}Se₂, J. Magn. Magn. Mater. 98, 37 (1991).
- [14] Bacsa, J., et al., Cation vacancy order in the $K_{0.8+x}Fe_{1.6-y}Se_2$ system: five-fold cell expansion accommodates 20% tetrahedral vacancies. Chem. Sci. DOI:10.1039/C1SC00070E
- [15] Bao, W. et al. A Novel Large Moment Antiferromagnetic Order in K_{0.8}Fe_{1.6}Se₂ Superconductor. arXiv: 1102.0830.
- [16] Yu, V., et al., Iron vacancy superstructure and possible room temperature antiferromagnetic order in superconducting Cs_vFe_{2-x}Se₂. Phys. Rev. B 83, 144410 (2011).
- [17] Bao, W. et al., Vacancy tuned magnetic high- T_c superconductor $K_x Fe_{2-x/2} Se_2$. arXiv: 1102.3674.
- [18] Harriger, L. W. et al., Nematic spin fluid in the tetragonal phase of BaFe₂As₂. arXiv:1011.3711.
- [19] Zhao, J. et al., Spin Waves and Magnetic Exchange Interactions in CaFe₂As₂. Nat. Phys. 5, 555 (2009).
- [20] Ewings, R. A. et al., Itinerant Spin Excitations in SrFe₂As₂ Measured by Inelastic Neutron Scattering. arXiv:1011.3831.
- [21] Lipscombe, O. J. *et al.*, Spin Waves in the $(\pi,0)$ Magnetically Ordered Iron Chalcogenide Fe_{1.05}Te. Phys. Rev. Lett. **106**, 057004 (2011).
- [22] Kamihara, Y., Watanabe, T., Hirano, M. and Hosono, H. Iron-based layered superconductor $La[O_{1-x}F_x]FeAs$ (x = 0.05-0.12) with $T_c = 26$ K, J. Am. Chem. Soc. **130**, 3296 (2008).
- [23] Maier, T. A., and Scalapino, D. J., Theory of neutron scattering as a probe of the superconducting gap in the iron pnictides. Phys. Rev. B **78**, 020514(R) (2008).
- [24] Korshunov, M. M. and Eremin, I., Theory of magnetic excitations in iron-based layered superconductors. Phys. Rev. B 78, 140509(R) (2008).
- [25] Christianson, A. D. et al., Resonant Spin Excitation in the High Temperature Superconductor Ba_{0.6}K_{0.4}Fe₂As₂. Nature 456, 930 (2008).
- [26] Seo, K., Bernevig, B. A., and Hu, J. P., Pairing Symmetry in a Two-Orbital Exchange Coupling Model of Oxypnictides. Phys. Rev. Lett. 101, 206404 (2008).
- [27] Cao, C. and Dai, J., Block Spin Ground State and 3-Dimensionality of (K,Tl)Fe_{1.6}Se₂. arXiv: 1102.1344.
- [28] You, Y. Z., Yao, H., and Lee, D.-H., The spin exictations of the block-antiferromagnetic K_{0.8}Fe_{1.6}Se₂. arXiv: 1103.3884v1.
- [29] Fang, C., Xu, B., Dai, P. C., Xiang, T., and Hu, J. P., Magnetic frustration and iron-vacancy ordering in iron chalcogenide. arXiv:1103.4599v2.
- [30] Lu, F., and Dai, X., Spin waves in the block checkerboard antiferromagnetic phase. arXiv:1103.5521
- [31] Yu, R., Goswami, P., and Si, Q., The magnetic phase diagram of an extended J_1 - J_2 model on a modulated square lattice and its implications for the antiferromagnetic phase of K_y Fe_xSe₂. arXiv:1104.1445v1.
- [32] Lester, C. et al., Dispersive spin fluctuations in the nearly optimally doped superconductor $Ba(Fe_{1-x}Co_x)_2As_2$ (x = 0.065). Phys. Rev. B **81**, 064505 (2010).
- [33] Si. Q., and Abrahams, E., Strong correlations and magnetic frustration in the high T_c iron pnictides. Phys. Rev. Lett. **101**, 076401 (2008).
- [34] Yu, W. Q. et al., 77 Se NMR study of pairing symmetry and spin dynamics in K_y Fe_{2-x}Se₂. Phys. Rev. Lett. **106**, 197001 (2011).

[35] Fang, C. et~al., Robustness of s-wave Pairing in Electron-Overdoped ${\rm A}_{1-y}{\rm Fe}_{2-x}{\rm Se}_2,$ arXiv:1105.1135.

SUPPLEMENTARY DATA

In addition to the spin wave data presented in the main text, we have taken triple-axis spectrometer measurements on HB-1 at Oak Ridge National Laboratory to determine the low-energy spin anisotropy gap. Before showing the results, we note that although the scattering cross section is related to the dynamic structure factor S(Q, E), it is proportional to the imaginary part of the dynamic susceptibility $\chi''(Q,\omega)$ if the temperature is much lower than the lowest energy spin waves. Theoretically, one has $S(Q,E) = 1/(1 - \exp(-E/(k_BT)))\chi''(Q,E)$. If $k_BT << E$ as is the case of the experiment, one has $S(Q,E) \propto \chi''(Q,E)$. Figure 5(a) shows $\chi''(Q,E)$ at $Q_{AF} = (0.6,0.2,3)$, which clearly establishes the anisotropy spin gap of \sim 8 meV. Constant energy scans at 5 meV and 10 meV shown in Fig. 5(b) confirm the presence of the spin gap below 8 meV. To further demonstrate the presence of spin gaps around 80 meV and 160 meV, we show in Figs. 5(c)-(e) constant energy cuts for energies of $E = 74 \pm 4$, 82 ± 4 , and 90 ± 4 meV, respectively. There are clearly no magnetic scattering near $E = 82 \pm 4$ meV [Fig. 5(d)]. Figures 5(f)-(h) show similar constant-energy images at $E = 140 \pm 10$, 155 ± 15 , and 195 ± 15 meV. The scattering near $E = 155 \pm 15$ meV are featureless, confirming the presence of a spin gap at this energy.

MODEL HEISENBERG HAMILTONIAN

The model we use to understand the magnetic excitation is a quantum spin model with up to third nearest neighbor (NNNN) exchange in the ab-plane, nearest neighbor (NN) exchange along the c-axis and a single ion anisotropy term, i.e.,

$$H = H_{ab} + H_c + H_s, \tag{1}$$

where

$$H_c = J_c \sum_r \mathbf{S}_r \cdot \mathbf{S}_{r+z},$$

$$H_s = \frac{J_s}{2} \sum_r (S_{r,x}^2 + S_{r,y}^2),$$
(2)

and H_{ab} is given in Ref. [1]. To solve the Hamiltonian, one can use standard linear spin wave approach. A generic position of the spin is given by

$$\mathbf{r} = m\mathbf{l_1} + n\mathbf{l_2} + \mathbf{d_i},\tag{3}$$

where m, n are integers and

$$\mathbf{l_1} = (2\mathbf{x} - \mathbf{y})/\sqrt{5},$$

$$\mathbf{l_2} = (\mathbf{x} + 2\mathbf{y})/\sqrt{5},$$

$$\mathbf{d_1} = 0, \ \mathbf{d_2} = \mathbf{x}, \ \mathbf{d_3} = \mathbf{x} + \mathbf{y}, \ \mathbf{d_4} = \mathbf{y}.$$

$$(4)$$

The Holstein-Primakoff transform (truncated) of the spin operators is given by For m + n =even:

$$S_{+}(\mathbf{r}) = \sqrt{2S}a_{i}(\mathbf{R}),$$

$$S_{-}(\mathbf{r}) = \sqrt{2S}a_{i}^{\dagger}(\mathbf{R}),$$

$$S_{z}(\mathbf{r}) = S - a_{i}^{\dagger}(\mathbf{R})a_{i}(\mathbf{R});$$
(5)

For m + n = odd:

$$S_{+}(\mathbf{r}) = \sqrt{2S} a_{i}^{\dagger}(\mathbf{R}),$$

$$S_{-}(\mathbf{r}) = \sqrt{2S} a_{i}(\mathbf{R}),$$

$$S_{z}(\mathbf{r}) = -S + a_{i}^{\dagger}(\mathbf{R}) a_{i}(\mathbf{R}).$$

$$(6)$$

Define $\psi^{\dagger}(k) = (a_1^{\dagger}(k), a_2^{\dagger}(k), a_3^{\dagger}(k), a_4^{\dagger}(k), a_1(-k), a_2(-k), a_3(-k), a_4(-k))$, and we have

$$H = \frac{1}{2} \sum_{k} \psi^{\dagger}(k) \begin{pmatrix} A(k) & B(k) \\ B(k) & A(k) \end{pmatrix} \psi(k). \tag{7}$$

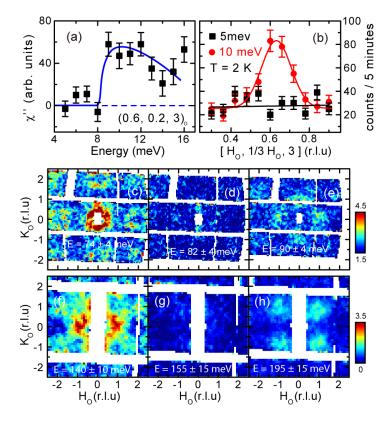


FIG. 5: Triple-axis spectrometer data obtained on HB-1 and additional spin-wave images near spin gaps on Rb_{0.89}Fe_{1.58}Se₂. (a) Constant-Q scan at the AF wave vector $Q_{AF}=(0.6,0.2,3)$ rlu with background subtracted, and corrected for Bose population factor. There is a clear spin gap below E=8 meV. (b) Constant-energy scans across the AF wave vector at E=5 meV and E=10 meV. The data confirm the presence of a spin gap at 5 meV. Spin wave images in the (H_o, K_o) plane for energy transfers of (c) $E=74\pm4$; (d) 82 ± 4 ; (e) 90 ± 4 ; (f) 140 ± 10 ; (g) 155 ± 15 ; 195 ± 15 meV. There are clearly no spin wave excitations at $E=82\pm4$ and 155 ± 15 meV.

A(k) and B(k) are four-by-four matrices, defined by:

$$A(k) = S \begin{pmatrix} E_0 & J_1 e^{ik_x} & J_2 e^{ik_x + ik_y} + J_3' e^{-i2k_x} & J_1 e^{ik_y} \\ \cdot & E_0 & J_1 e^{ik_y} & J_2^{-ik_x + ik_y} + J_3' e^{-2ik_y} \\ \cdot & \cdot & E_0 & J_1 e^{-ik_x} \\ \cdot & \cdot & \cdot & E_0 \end{pmatrix},$$
(8)

$$B(k) = S \begin{pmatrix} 2J_c \cos(k_z) & J_2' e^{-ik_x + ik_y} + J_3 e^{-2ik_y} & J_1' e^{-ik_y} & J_2' e^{-ik_x - ik_y} + J_3 e^{2ik_x} \\ & 2J_c \cos(k_z) & J_2' e^{-ik_x - ik_y} + J_3 e^{2ik_x} & J_1' e^{ik_x} \\ & & 2J_c \cos(k_z) & J_2' e^{ik_x - ik_y} + J_3 e^{2ik_y} \\ & & & 2J_c \cos(k_z) & 2J_c \cos(k_z) \end{pmatrix},$$
(9)

where $E_0 = -(2J_1 + J_2 - J_1' - 2J_2' - 2J_3 + J_3' - 2J_c - J_s)S$. The lower triangle elements are suppressed because both matrices are hermitian.

We use equations of motion to solve this Hamiltonian.

$$\partial \psi(k)/\partial t = -i \begin{pmatrix} A(k) & B(k) \\ -B(k) & -A(k) \end{pmatrix} \psi(k). \tag{10}$$

Solving this eigenvalue problem for each k, we have

$$H = \sum_{i=1,2,3,4:k} (\gamma_i^{\dagger}(k)\gamma_i(k) + 1/2)\omega_i(k), \tag{11}$$

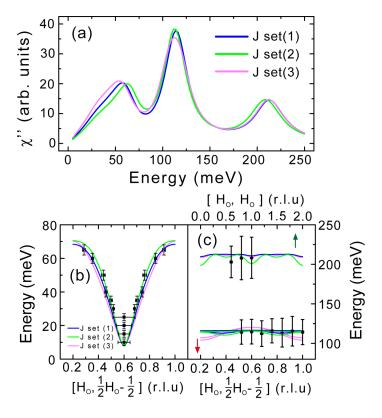


FIG. 6: (a) Energy dependence of imaginary part of local susceptibility for the three different exchange parameter sets. (b,c) Dispersion curves for the three different exchange parameter sets as discussed in the text.

and

$$a_i(k) = \sum_j U_{ij}(k)\gamma_j(k) + V_{ij}(k)\gamma_j^{\dagger}(-k). \tag{12}$$

The differential cross section of inelastic neutron scattering can be expressed in terms of the spin wave dispersion and wave functions:

$$\sigma(\omega, q) = I_0(\omega, q)(1 + n_B(\omega, T)) \sum_{\alpha} |\sum_{i} U_{i\alpha}(q) + V_{i\alpha}^{\star}(-q)|^2 D(\omega, \omega_{\alpha}).$$
(13)

In the above expression, $I_0(\omega, q)$ includes all factors of experimental resolution extracted from information of each detector, $n_B(\omega, T)$ is the Bose factor and $D(\omega, \omega_\alpha)$ is the harmonic oscillator damping given by

$$D(\omega, \omega_0) = \frac{4}{\pi} \frac{\omega \omega_0 \Gamma(\omega)}{(\omega^2 - \omega_0^2)^2 + 4\Gamma(\omega)^2 \omega^2}.$$
 (14)

The damping strength $\Gamma(\omega)$ is approximated by a linear function of energy whose explicit form is to be fitted. Our fitting is based on so far the most general spin model with all symmetry allowed exchanges up to NNNN. A failure of this model in understanding the data would mean that the observed excitations cannot be explained by a local moment picture and the effect of itinerant electrons must be seriously considered.

FITTING CONSTRAINTS

The high quality of the data allows one to place quantitative constraints on parameters in the model. The data shows that the excitations exist in three separate energy ranges. The lowest branch starts from ~ 9 meV to ~ 70 meV, second from ~ 100 meV to ~ 140 meV and the third branch from ~ 180 meV to ~ 230 meV. The low energy part of the first branch can be fitted very well by the form

$$\epsilon(k) = \sqrt{\Delta_s^{exp2} + v_s^{exp2} k^2},\tag{15}$$

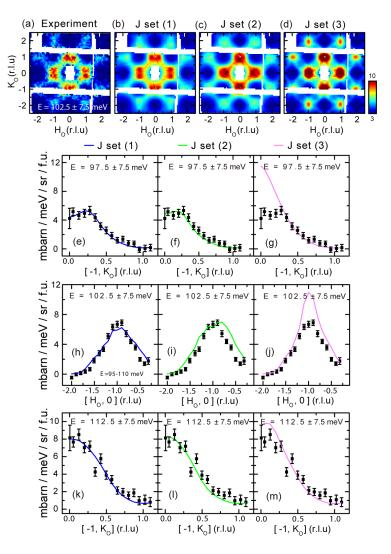


FIG. 7: Calculated dynamic structure factor and their comparison with Heisenberg Hamiltonian with different exchange parameters. (a) Constant energy cut of data at $E = 102.5 \pm 7/5$ meV projected onto the (H_o, K_o) plane. (b,c,d) Calculated dynamic structure factor $S(q, \omega = 102.5 \pm 7/5)$ projected onto the (H_o, K_o) plane for three different exchange coupling parameters. (e-m)Cuts along different directions and their comparison with spin wave calculations in three different exchange coupling parameters.

with $v_s^{exp} = 300 \text{ meV} \cdot \text{Å}$ and $\Delta_s^{exp} = 9 \text{ meV}$. At the propagation vector of the ground state Q = (0.6, 0.2, 1) rlu (in the orthorhombic basis), energy has k_z dispersion, and the band top is about $E_c^{exp} \sim 30 \text{ meV}$. All these values have analytical expressions in the spin wave model. The anisotropy gap (bottom of the first branch) is

$$\Delta_s = S\sqrt{J_s(2J_1' + 4J_2' + 4J_3 + 4J_c + J_s)}. (16)$$

The top of the first band is reached at $Q_o = (0.2, 0.4, 0)$ rlu with

$$E_{1t} = 2S[2J_1^2 + J_1'(J_2' + J_3 - J_3' + J_c) + (J_2' + J_3 - J_3')(J_2' + J_3 - J_3' + 2J_c) - J_1(J_1' + 2(J_2' + J_3 - J_3' + J_c))$$
(17)
$$-\sqrt{4J_1^4 + {J_1'}^2 J_c^2 + 4J_1^2(J_2' + J_3 - J_3' + J_c)(J_1' + J_2' + J_3 - J_3' + J_c) - 4J_1^3(J_1' + 2(J_2' + J_3 - J_3' + J_c))}]^{\frac{1}{2}}.$$

Without single ion anisotropy, i.e., $J_s = 0$, the spin wave velocity is given by

$$v_s = \sqrt{\frac{5}{2}} S\{ [J_1(J_1' + 2(J_2' + J_3 - J_3')) + J_1'(J_2 - J_2' - J_3 + J_3') + 2(J_2(J_2' + J_3 - J_3') + 2J_3(J_3' - J_2'))]$$

$$(J_1' + 2(J_2' + J_3 + J_c)) / (J_1 - J_1' + J_2 - J_2' - J_3 + J_3')\}^{1/2}.$$
(18)

The expression with $J_s \neq 0$ is also available but too lengthy to be placed here, and interested readers can request it from the authors. The second branch actually contains two close spin wave bands. The branch starts at Q = (0.3, 0.1, 1) rlu with energy E_{2b} , whose expression is again too lengthy to be published. The second branch ends at $\Gamma = (0,0,0)$ point with

$$E_{2t} = S\sqrt{(2J_1 - 2J_1' + 2J_2 - 2J_2' - 2J_3 + 2J_3' - J_s)(2J_1 + 2J_2 - 2J_2' - 2J_3 + 2J_3' - 4J_c - J_s)}.$$
 (19)

The highest branch starts at Γ point with

$$E_{3b} = S\sqrt{(4J_1 - 4J_2' - 4J_3 - J_s)(4J_1 - 2J_1' - 4J_c - J_s)},$$
(20)

and ends at (0.2, 0.4, 0) with

$$E_{3t} = 2S[2J_1^2 + J_1'(J_2' + J_3 - J_3' + J_c) + (J_2' + J_3 - J_3')(J_2' + J_3 - J_3' + 2J_c) - J_1(J_1' + 2(J_2' + J_3 - J_3' + J_c)) (21) + \sqrt{4J_1^4 + {J_1'}^2 J_c^2 + 4J_1^2(J_2' + J_3 - J_3' + J_c)(J_1' + J_2' + J_3 - J_3' + J_c) - 4J_1^3(J_1' + 2(J_2' + J_3 - J_3' + J_c))]^{\frac{1}{2}}}.$$

The band top along the c-axis is reached at (0.6, 0.2, 0) with

$$E_c = S\sqrt{[2(J_1' + 2J_2' + 2J_3) - J_s](4J_c + J_s)}.$$
(22)

Based on the data and considering the effect of large damping at high energies, we have for the above quantities the following constraints:

$$\Delta_{s} = \Delta_{s}^{exp} = 8 \sim 12 \text{ meV},$$

$$v_{s} = v_{s}^{exp} = 250 \sim 300 \text{ meV} \cdot \text{Å},$$

$$E_{1t} = 60 \sim 75 \text{ meV},$$

$$E_{2b} = 90 \sim 110 \text{ meV},$$

$$E_{2t} = 110 \sim 130 \text{ meV},$$

$$E_{3b} = 180 \sim 200 \text{ meV},$$

$$E_{3t} = 200 \sim 220 \text{ meV},$$

$$E_{c} = 25 \sim 30 \text{ meV}.$$
(23)

FITTING PARAMETERS

The above constraints give a very narrow range of parameters, we can further constraint possible exchange constants so that a quantitative fit to the data shown in the paper can be found. In this section we discuss what elements are indispensable to our fittings.

We first emphasize that a proper fitting should have $J_3 > 0$ and $J'_1 > 0$ (antiferromagnetic). To see this, we compare the following possible parameters since they can all approximately describe the data:

(1) $SJ_1 = -36$, $SJ_1' = 15$, $SJ_2 = 12$, $SJ_2' = 16$, $SJ_3 = 9.5$, $SJ_3' = 0$, $SJ_c = 1.4$, $SJ_s = 0.44$ meV. (2) $SJ_1 = -36$, $SJ_1' = -5.7$, $SJ_2 = 13.4$, $SJ_2' = 22.4$, $SJ_3 = 14.2$, $SJ_3' = 0$, $SJ_c = 1.4$, $SJ_s = 0.44$ meV. (3) $SJ_1 = -36$, $SJ_1' = 10$, $SJ_2 = 11$, $SJ_2' = 28.7$, $SJ_3 = 0$, $SJ_3' = 0$, $SJ_c = 1.4$, $SJ_s = 0.44$ meV. Figure 6 summarizes the calculated $\chi''(\omega)$ and spin wave dispersions for all three sets of parameters. From the calculation, we see that all three parameter sets give similar local susceptibilities, and therefore cannot be distinguished based on $\chi''(\omega)$ alone.

By comparing the calculated spin wave dispersion curves with data, we were able to separate which model is correct. Figure 6(b) and (c) shows the outcome for the three sets of exchange couplings for the acoustic and optical modes, respectively. We see that parameters of (1) and (2) fit the acoustic and optical data slightly better. Although the imaginary part of local susceptibility and dispersion curves for different exchange parameter sets are similar, their constant energy patterns at ~110 meV are very different, which provides key clues to the choice among different exchange coupling parameters. In the energy range around 110 meV, several optical branches are mixed together. The combined spin wave intensity patterns depend sensitively on the exchange coupling parameters. Figure 7 compares directly the calculated patterns with the observation for the three set of exchange parameters. Clearly, the first set of parameters describes the data much better. This is what we have used to determine the effective magnetic exchange

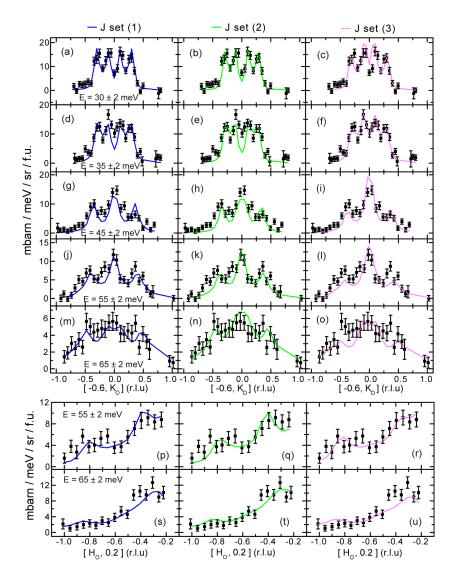


FIG. 8: Spin-wave dispersions of $Rb_{0.89}Fe_{1.58}Se_2$ and fits using Heisenberg Hamiltonian with three different exchange coupling parameters as discussed in the text. Spin-wave dispersions in the acoustic branch obtained by cutting along high-symmetry directions and model fits using three different sets of exchange coupling parameters (a)-(o) Cuts along the $[-0.6, K_o]$ direction by integrating H_o from -0.65 to -0.55. (p)-(u) Cut along $[H_o, 0.2]$ direction by integrating K_o from 0.15 to 0.25.

coupling constants. This conclusion is further confirmed by comparing the calculated dispersion with the observed dispersion using the three sets of parameters as shown in Figs. 7, 8 and 9.

As a remark, we note the important fact that the in-block NNN exchange J_2 must be positive (antiferromagnetic) for all candidate sets of parameters. J_2 has little effect on the first and the third branches of dispersion, but is strongly coupled to the middle branch. A ferromagnetic J_2 can push up the second branch for about 30%. This means the gap between first and second branches would be more than 40 meV, while in experiment it is clearly less than 30 meV.

SUM RULE

Here we discuss the total moment sum rule. For a Heisenberg model with spin S, the sum rule is formulated as Ref. [2]:

$$M_o = \frac{1}{N} \sum_{\alpha} \int d\mathbf{k} \int_{-\infty}^{\infty} d\omega S^{\alpha\alpha}(\mathbf{k}, \omega) = M_x + M_y + M_z = g^2 \mu_B^2 S(S+1), \tag{24}$$

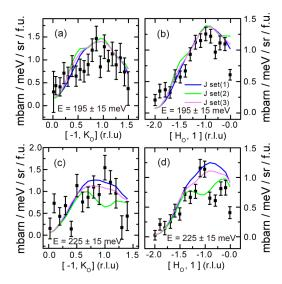


FIG. 9: Spin-wave cuts of $Rb_{0.89}Fe_{1.58}Se_2$ and fits using Heisenberg Hamiltonian with three sets of parameters. Q-cuts for the highest branch. The H_o integration range in (a),(c) is from -1.05 to -0.95. Integration of the K_o range in (b),d) is from 0.8 to 1.2.

where g is the Lande factor. For free electrons g=2. In Rb_{0.89}Fe_{1.58}Se₂, the maximum possible spin S=2 is expected, which gives $M_o=24~\mu_B^2/{\rm Fe}$.

The longitudinal part M_z comes from the static moment (elastic) and the inelastic contribution. For our system, the static moment is about 3 μ_B / Fe [3], which contributes 9 μ_B^2 /Fe. The inelastic part mainly comes from the two-magnon scattering process. The magnetization reduction can be evaluated as $\Delta S = 0.5$ from the static moment for S = 2. From Ref. [2], we can estimate the two-magnon spectral weight as $\Delta S(1 + \Delta S)g^2\mu_B^2 \simeq 3\mu_B^2$ /Fe, where the normalization factor has been chosen as 1. The spectral weight from the two-magnon process is only 1/3 of the elastic part, which is much weaker than the cuprates which has S = 1/2. In unpolarized neutron experiments, the two-magnon spectral weight is generally very hard to detect. We will ignore it in the following treatment.

The transverse part $M_x + M_y$ mainly comes from the one-magnon spin wave spectrum. According to Eq. (1) in Ref. [4], we can get the dynamic structure factor S(E) by removing the magnetic form factor. Then using Eq. (5) in Ref. [4], we can get the transverse part by integrating S(E) over the whole energy range. Experimentally we do not observe the neutron scattering signal above 250 meV, so we can choose the integration range from 8 to 250 for the inelastic signal only. We get the transverse part $\sim 26 \pm 5~\mu_B^2 (f.u.)^{-1}$, where f.u. means formula unit. Considering the formula of $\mathrm{Rb}_{0.89}\mathrm{Fe}_{1.58}\mathrm{Se}_2$, we divide it by a factor of 1.6. The transverse part $M_x + M_y$ is evaluated as $16 \pm 3\mu_B^2/Fe$.

The total moment from our evaluation is $25 \pm 5 \ \mu_B^2/\text{Fe}$, which is very close to the expected total moment from the sum rule. Thus the Heisenberg model with S=2 is an appropriate description for the insulating Rb_{0.89}Fe_{1.58}Se₂ and the spin waves describe the spin dynamics very well.

^{*} Electronic address: pdai@utk.edu

^[1] Fang, C., Xu, B., Dai, P. C., Xiang, T., and Hu, J. P., Magnetic frustration and ion-vacancy ordering in iron chalcogenide. arXiv:1103.4599v2.

^[2] Lorenzana, L., Seibold, G., and Coldea, R., Sum rules and missing spectral weight in magnetic neutron scattering in the cuprates. Phys. Rev. B 72, 224511 (2005).

^[3] Bao, W. et al. A Novel Large Moment Antiferromagnetic Order in K_{0.8}Fe_{1.6}Se₂ Superconductor. arXiv: 1102.0830.

^[4] Lester, C. et al., Dispersive spin fluctuations in the nearly optimally doped superconductor Ba(Fe_{1-x}Co_x)₂As₂ (x = 0.065). Phys. Rev. B **81**, 064505 (2010).